

Green Synthesis of Iron Nanozymes Using *Eucalyptus grandis* Extract and Their Application as Peroxidase-Like Catalysts for H₂O₂ Quantification

Luísa F. M. Mazzini,^a Guilherme Mateus Bousada,^a Gustavo A. Puiatti^b and Renata P. L. Moreira^{ib}*,^a

^aDepartamento de Química, Universidade Federal de Viçosa, 36570-000 Viçosa-MG, Brazil

^bDepartamento de Engenharia Civil, Universidade Federal de Viçosa, 36570-000 Viçosa-MG, Brazil

In this work, iron nanoparticles were synthesized by a green and bio-inspired process, using *Eucalyptus grandis* extract as a reducing and stabilizing agent. The functional groups from the extract were incorporated into the structure of the nanoparticles, as confirmed by infrared spectroscopy. Characteristic peaks of zero-valence iron were observed by X-ray diffraction analysis, besides hematite and goethite. The nanoparticles showed spherical morphology and an average size of 96.4 nm. The zeta potential ($|35|$ mV) indicated good stability. The nanoparticles were used as catalysts for *o*-phenylenediamine oxidation by H₂O₂, exhibiting optimal catalytic activity. The kinetic assays were performed, and the Michaelis-Menten model was adjusted to the data (maximum rate reached (V_{\max}) = 2.0 $\mu\text{mol L}^{-1} \text{s}^{-1}$ and Michaelis-Menten constant (K_m) = 307 $\mu\text{mol L}^{-1}$). A spectrophotometric method was developed for H₂O₂ quantification. The analytical curve (18.3-112.6 $\mu\text{mol L}^{-1}$) showed a good linear fit and limits of detection and quantification of 5.48 and 18.3 $\mu\text{mol L}^{-1}$, respectively. Thus, the method is very promising, adhering to the principles of green chemistry.

Keywords: green chemistry, sustainability, nanomaterials, *o*-phenylenediamine, *Eucalyptus grandis*

Introduction

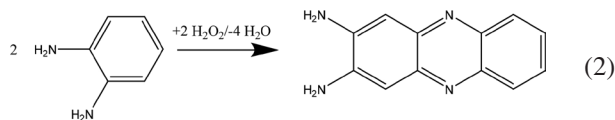
Hydrogen peroxide is a versatile chemical with widespread applications in food processing, pharmaceuticals, and chemical industries.^{1,2} However, in living organisms, it is a toxic metabolite that can cause damage to cells. The biological process of detoxification of hydrogen peroxide by the enzyme catalase, an enzyme from the peroxidase group, involves the conversion of hydrogen peroxide into water and molecular oxygen, as shown in equation 1.³



Enzymes from the peroxidase group are widely used as biosensors in colorimetric methods due to their high selectivity and catalytic efficiency, being sensitive to the detection of H₂O₂.⁴ Despite the many benefits of using enzymes, their widespread application is limited due to their

susceptibility to adverse environmental conditions, such as high temperatures, pH changes, and other factors that can lead to enzyme denaturation.⁵ In addition, peroxidases have a high cost of production, purification, and acquisition.^{1,6-8} Therefore, the synthesis of nanomaterials that mimic enzymes, also called nanozymes, has been an attractive alternative due to their higher stability and low cost.^{6,7,9}

The use of *o*-phenylenediamine (OPD) is an interesting tool to detect hydrogen peroxide. This colorless compound is oxidized in the presence of oxygen or hydrogen peroxide, forming 2,3-diaminophenazine (DAP) (equation 2) with a yellowish color.¹⁰ However, the reaction is slow, requiring the use of catalysts.¹⁰



Among the catalysts, nanoparticles of transition metals (e.g., iron) stand out due to their wide applicability and versatility. The synthesis of iron nanoparticles can be performed quickly and easily. Besides, they have very

*e-mail: renata.plopes@ufv.br

Editor handled this article: Jaísa Fernandes Soares

favorable chemical properties, being highly reactive and able to donate electrons.¹¹ Despite these advantages, nanoparticles tend to aggregate easily, reducing their reactive sites.¹² To overcome this challenge, plant extracts were proposed as an alternative to synthesizing iron-based nanoparticles.¹³ Because of this reliance on biological resources, the use of plant extracts in the synthesis of metal nanoparticles can be considered bio-inspired.¹⁴ In addition, the use of non-toxic and non-hazardous reducing agents also follows the principles of green chemistry.¹³

Green synthesis using plant extracts has gained notoriety due to its low cost, reduced use of toxic chemicals, and low energy consumption.^{15,16} In these processes, plant extraction is usually performed using solvents, among which water is the most used.¹² The phytochemicals found in the extracts, such as flavonoids and terpenoids, can produce and stabilize nanoparticles by reducing aggregation, due to the presence of functional groups such as carboxylic acids, phenols, and aldehydes.¹² Studies¹² have used iron nanoparticles synthesized by plant extracts. Typically, this synthesis involves mixing a plant extract with iron precursors, which are then reduced, causing a change in the color of the system.¹²

Building on the previous studies mentioned,^{12,13} the present work aims to develop a spectrophotometric method for the detection and quantification of hydrogen peroxide based on the oxidation reaction of OPD, using iron nanoparticles synthesized by a green and bio-inspired process as a peroxidase-like catalyst.

Experimental

Standards and reagents

In this work, analytical grade reagents were used. The citric acid (99.5%), sodium hydroxide (99.67%) and ethanol (96.24%) were purchased from Neon (Suzano, Brazil). The *o*-phenylenediamine (OPD) (98%) was purchased from Merck (São Paulo City, Brazil). Hydrochloric acid (37% v/v), hydrogen peroxide (30% v/v), methanol (95%) and chloroform (99.8%) were acquired from Alfhatec (São Bernardo do Campo, Brazil). Iron(II) sulfate heptahydrate (99-101%) was obtained from Química Moderna (Barueri, Brazil). The *t*-butyl alcohol (99%) was obtained from Êxodo Científica (Sumaré, Brazil). The isopropyl alcohol (99.5%) was purchased from Vetec (Rio de Janeiro City, Brazil). The sodium azide (99%) was purchased from Anidrol (Pindamonhangaba, Brazil).

All aqueous solutions were prepared with type 1 water from the Milli-Q system (Millipore Corporation) and stored under refrigeration (4 °C).

Obtaining and preparing *Eucalyptus grandis* leaves

Eucalyptus grandis leaves were collected from trees on a rural property in Viçosa, Minas Gerais, Brazil (42.94° W 20.82° S). The leaves were washed with distilled water, dried in an oven at 60 °C for three consecutive days, ground in a Wiley knife mill (Tecnal TE680, Piracicaba, Brazil), and sieved (30 mesh sieve). The processed samples were then stored in a light-protected desiccator at room temperature.

Obtaining the reducing extract from *Eucalyptus grandis* leaves

The reducing extract was obtained from *Eucalyptus grandis* leaves following the method described by Puiatti *et al.*¹⁷ The leaves were rinsed with distilled water and then dried at 60 °C for three consecutive days. Later, the leaves were pulverized using a Wiley knife mill (Tecnal TE680; Piracicaba, Brazil) and then sifted through a 30-mesh sieve. The prepared samples were kept in a desiccator at room temperature, and shielded from light. Then, 6.00 g of processed leaves were added to 100 mL of type 1 water and stirred at 80 °C for 1 h. The obtained mixture was filtered under vacuum, giving a brown-colored extract. The extract was diluted with type 1 water to a final volume of 100 mL.

Synthesis of iron nanoparticles (FeNPs)

The nanoparticles were synthesized using the protocol described by Puiatti *et al.*¹⁷ Thus, the freshly prepared reducing extract (100 mL) was added dropwise to FeSO₄ solution (50 mL, 0.100 mol L⁻¹). The system was submitted to magnetic agitation at room temperature during the addition of the extract. The resulting suspension (theoretical iron concentration of 33.3 mmol L⁻¹) was stored under refrigeration (ca. 4 °C) until further use.

Characterization

The conductance of the plant extract and the suspension of FeNPs were measured using a conductivity meter AZ[®], model 86503 (Taichung, Taiwan). The pH was determined using a pH meter equipped with a combination glass electrode, Mettler Toledo, model Five Easy Plus (Barueri, Brazil). Finally, the redox potential was determined using a potentiometer, HANNA, model pH 21-02 (Barueri, Brazil).

The X-ray diffraction analysis (XRD) for the nanoparticles was carried out in a D8-Discover-Bruker

equipment (Billerica, USA), equipped with a copper tube (1.5418 Å), ranging from $2\theta = 10$ to 50° with a 0.05° step. The nanoparticle suspension was dropped onto a glass slide and left to dry at room temperature.

Fourier-transform infrared spectroscopy (FTIR) was also used to analyze the plant extract obtained from eucalyptus leaves and the suspension of FeNPs, Varian 660-IR equipment and GladiATR diamond crystal, 400 to 4000 cm^{-1} range (Palo Alto, USA). To prepare the samples, the plant extract or the FeNPs suspension were dripped onto Petri dishes. Then, the dishes were left to dry at room temperature.

Scanning electron microscopy (SEM) analyses were performed using a JSM-6010LA-JEOL equipment operated at 15 kV (Akishima, Japan). The FeNPs suspensions were previously diluted with type 1 water (dilution 1:100 v/v). The resulting suspension was dripped into the sample holder (stub). After drying at room temperature, the sample was coated with a gold film using Quorum Q150R S equipment.

Thermogravimetric analysis (TGA) was conducted utilizing the Simultaneous Thermal Analyzer 6000 equipment from PerkinElmer (Waltham, USA). Before the study, the FeNPs suspension underwent drying in an oven at $40\text{ }^\circ\text{C}$ for 8 h. The material was then subjected to heating, ranging from 30 to $900\text{ }^\circ\text{C}$, at a heating rate of $10\text{ }^\circ\text{C min}^{-1}$.

The transmission electron microscopy (TEM) analyses coupled with energy dispersive spectroscopy (EDS) were carried out using the JEM-2100-JEOL equipment (Tokyo, Japan). This equipment is equipped with a LaB_6 electron emission source and operated at an accelerating voltage of 200 kV. The FeNPs suspension was deposited onto a copper grid coated with Formvar/carbon. The nanoparticle sizes were determined using the ImageJ software,¹⁸ measuring 25 randomly selected particles from the image.

The dynamic light scattering (DLS) analyses were conducted using the Litesizer 500 equipment, Anton Paar (Graz, Austria), operating at angles of 15, 90, and 175° within a range from 0.3 nm to 10 μm . Before analysis, the FeNPs suspension was diluted with type 1 water and subjected to sonication for 2 min.

Finally, the zeta potential of FeNPs at different pH values was determined using the Malvern Zetasizer Nano ZS90 equipment (Malvern, UK). The samples (25 μL of FeNPs suspension) were added to a sodium chloride solution (1:400 v/v dilution) at 1.00 mmol L^{-1} to adjust the ionic strength of the medium.¹⁹ Finally, the pH was adjusted to different values (2, 3, 4, 5, 6, 7, 8, 9, 10, and 11) using HCl or NaOH solutions, both at 0.100 mol L^{-1} .²⁰

General procedure of o-phenylenediamine oxidation mediated by FeNPs

The reaction was conducted in a quartz cuvette of 1.00 cm optical path. Then, 2.85 mL of citrate buffer solution (0.100 mol L^{-1}) at pH 3.00 were added into the cuvette, followed by 200 μL of OPD solution (10.0 mmol L^{-1}), 100 μL of hydrogen peroxide 30% (v/v), and 250 μL of FeNPs suspension (4.165 mmol L^{-1}). The total final volume was 3.40 mL. The FeNPs suspension was previously sonicated for 5 min. The reaction was monitored for 35 min at room temperature by molecular absorption spectrophotometry in the UV-Vis region using Evolution Array UV-Visible Spectrophotometer from Thermo Fisher Scientific (Waltham, Massachusetts, USA). The absorbance data were then converted to DAP concentration using the molar absorptivity coefficient ($\lambda = 451\text{ nm}$, $\log \epsilon_{451} = 4.33$).²¹

Method optimization

The optimal conditions were determined using the procedure described above, varying one parameter at a time. For the pH evaluation, citrate buffer solutions (0.100 mol L^{-1}) were prepared at three different pH values (3.00, 5.00, and 7.00). Then, 2.85 mL of the citrate buffer at pH 3.00, 5.00 or 7.00 were added into the cuvette, followed by the addition of 200 μL of OPD solution (10.0 mmol L^{-1}), 100 μL of hydrogen peroxide 30% (v/v), and 250 μL of FeNPs suspension (4.165 mmol L^{-1}) previously sonicated for 5 min. The reaction was monitored for 35 min.

For the FeNPs dose evaluation, different dosages of the suspension, such as 0.0610, 0.122, 0.184, 0.245, 0.306 and 0.368 mmol L^{-1} , were prepared. Then, 2.85 mL of the citrate buffer solution (0.100 mol L^{-1}) at pH 3.00 were added into the cuvette, followed by the addition of 200 μL of OPD solution (10.0 mmol L^{-1}), 100 μL of hydrogen peroxide 30% (v/v), and 250 μL of FeNPs suspension in the desired dosage, previously sonicated for 5 min. The reaction was monitored for 35 min.

For the OPD concentrations evaluation, different concentrations of this compound, such as 73.5, 147.1, 294.1, 441.2, 588.2 and 735.3 $\mu\text{mol L}^{-1}$, were employed. Then, 2.85 mL of the citrate buffer solution (0.100 mol L^{-1}) at pH 3.00 were added into the cuvette, followed by the addition of 200 μL of OPD solution at desired concentration, 100 μL of hydrogen peroxide 30.0% (v/v), and 250 μL of FeNPs suspension (4.165 mmol L^{-1}) previously sonicated for 5 min. The reaction was monitored for 35 min.

Hydrogen peroxide analytical curve

The H_2O_2 analytical curve was prepared from 16.8 to

112.7 $\mu\text{mol L}^{-1}$ using the optimal conditions described in “Method optimization” sub-section. Thus, 100 μL of hydrogen peroxide 30% (v/v), followed by 200 μL of OPD solution (10.0 mmol L^{-1}), were added with 2.85 mL citrate buffer solution (0.100 mol L^{-1}) at pH 3.00 and 250 μL of FeNPs suspension (4.165 mmol L^{-1}). The model quality of the linear regression was evaluated by the coefficient of determination (R^2) and residuals plot. The measurements were performed in triplicate. The limits of quantification (LOQ), detection (LOD), and analytic resolution (AnR) were determined according to equations 3-5.

$$\text{LOD} = 3 \times \frac{\text{SD}}{S} \quad (3)$$

$$\text{LOQ} = 10 \times \frac{\text{SD}}{S} \quad (4)$$

$$\text{AnR} = 3 \times \frac{\text{SDr}}{S} \quad (5)$$

where SD is the standard deviation of the blank, SDr is the standard deviation of the residues and S is the analytical sensitivity.

Michaelis-Menten model

The reaction kinetics was evaluated following the same procedure described in the previous sections, using the optimal concentrations found and monitoring the signal at 451 nm for 35 min. The variation of absorption over time represented the speed of the reaction. The assays were performed in triplicate. The kinetic parameters were determined from the Michaelis-Menten model (equation 6).

$$V_0 = \frac{V_{\text{Max}} \times [S]}{K_m + [S]} \quad (6)$$

where V_0 is the initial reaction rate, V_{max} is the maximum rate reached, K_m is the Michaelis-Menten constant, and $[S]$ is the substrate concentration.

Investigation of the reaction mechanism

To propose a possible mechanism for the oxidation reaction of OPD by H_2O_2 mediated by FeNPs, a study using radical inhibitors was performed. The solutions of methanol ($\cdot\text{OH}$ inhibitor), ethanol ($\cdot\text{OH}$ inhibitor), isopropyl alcohol ($\cdot\text{OH}$ inhibitor), *t*-butyl alcohol ($\cdot\text{OH}$ inhibitor) and sodium azide ($^1\text{O}_2$ inhibitor) were prepared at the concentration six times higher than the H_2O_2 concentration. The inhibitor stock

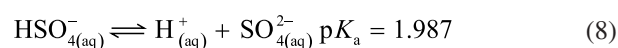
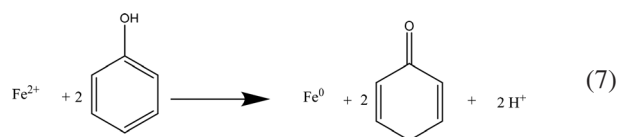
solution was prepared with citrate buffer (0.100 mol L^{-1}) at pH 3.00. Then, 2.85 mL of the citrate buffer solution (0.100 mol L^{-1}) at pH 3.00 containing the inhibitors (80.3 mmol L^{-1}), 200 μL of OPD solution (10.0 mmol L^{-1}), 100 μL of hydrogen peroxide (381.4 mmol L^{-1}) and 250 μL of FeNPs (4.165 mmol L^{-1}) were added in a cuvette, respectively. The assays were performed individually for each inhibitor. All assays were performed in replicate. The reaction was monitored for 35 min.

Results and Discussion

Characterization

Figure S1 (Supplementary Information (SI) section) shows the FeSO_4 aqueous solution (0.100 mol L^{-1}), the *Eucalyptus grandis* aqueous extract, and the FeNPs suspension. The plant extract has a brown color, whereas the FeNPs suspension has a black color. This color change can be attributed to the reduction of Fe^{2+} to Fe^0 .^{22,23} The formation of FeNPs was monitored by tracking changes in conductance and redox potential throughout the reaction, as shown in Figure S2 (SI section). The decrease in the solution conductivity can be attributed to the formation of FeNPs through the reduction of Fe^{2+} to Fe^0 (Table 1). Additionally, changes in the redox potential were also observed, indicating a decrease in the oxidation state of the iron(II) ions during the reaction (Table 1). Such findings are also in accordance with Pourbaix’s diagram for the iron-water system (Figure S3, SI section), which shows that when there is a decrease in the redox potential for pH values close to 2-3, iron is reduced from Fe^{2+} to Fe^0 .^{24,25} The general description of the reduction Fe^{2+} ions by phenol is shown in the equation 7.^{17,26}

Equation 7 shows that H^+ ions are released in the system as a result of the reaction. However, the pH remains relatively constant (2.37-2.49, Table 1) even though the plant extract used in the experiment had a pH of 4.95. This could be due to the acid-base character of the bisulfate ion from the FeSO_4 aqueous solution (equation 8), which has a $\text{p}K_a$ value of 1.987. This creates a buffer region between pH 0.98 to 2.98 where pH values are relatively stable.



Zeta potential (ζ) results are shown in Figure S4 (SI section). Surface charge is an important indicator of the

Table 1. Conductance, redox potential, and pH for the *Eucalyptus grandis* aqueous extract, iron sulfate solution, and FeNPs suspension

Sample	Conductance / ($\mu\text{s cm}^{-1}$)	Redox potential / mV	pH
<i>E. grandis</i> plant extract	766	118	4.95
FeSO ₄ (0.100 mol L ⁻¹)	8640	245	2.37
FeNPs suspension	4040	220	2.49

FeNPs: iron nanoparticles.

stability and reactivity of nanoparticles.^{27,28} The FeNPs displayed a negative charge ($\zeta = -2.15$ to -35.2) for all pH values examined. To maintain stability, nanoparticles require $|\zeta| \geq 30$ mV. In this condition, the repulsive forces are large enough to prevent their aggregation.¹⁷ The FeNPs suspension showed a zeta potential of approximately -35 mV in the pH range between 5 and 10, indicating that they are likely to remain stable under these conditions with respect to aggregation. The relationship between zeta potential and pH can be explained by the protonation/deprotonation of functional groups present on the surface of the material, such as hydroxyl ($-\text{OH}$) and carboxylic acids ($-\text{COOH}$).²⁰

The FTIR spectra obtained for the plant extract of *E. grandis* and the FeNPs are shown in Figures S5 (SI section) and 1, respectively. Both spectra have bands in common. The band at 3270 cm^{-1} can be attributed to the stretching of the O–H bond.²⁶ The band at 2930 cm^{-1} can be attributed to the symmetric and asymmetric stretching of C–H bonds of methyl and alkyl groups.^{26,29} The band at 1714 cm^{-1} can be attributed to the C=O stretching of carbonyl groups derived from carboxylic acids.¹⁷ The band around 1610 cm^{-1} can be attributed to C=C elongation and tensile vibrations in aromatic rings of polyphenolic compounds.²⁶ The band at 1446 cm^{-1} is associated with the aliphatic C–H bond and the aromatic ring stretching vibration, attributed to phenolic compounds.²⁶

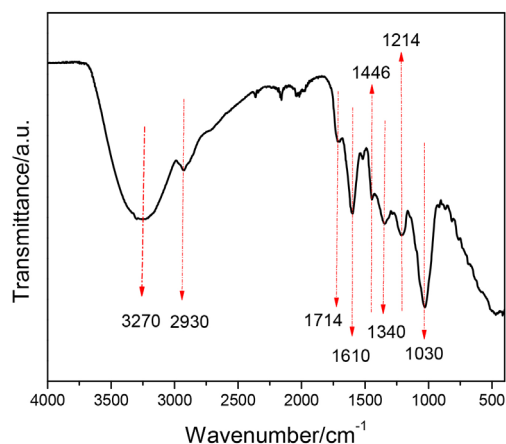


Figure 1. Fourier transform infrared-attenuated total reflectance (FTIR-ATR) of FeNPs (iron nanoparticles) synthesized through a green process utilizing *Eucalyptus grandis* leaf extract.

The FTIR analysis revealed the presence of carboxylic acids and phenols in both the extract of *E. grandis* leaves and the FeNPs suspension, consistent with Oliveira *et al.*³⁰ findings. They synthesized silver nanoparticles using *E. grandis* leaves extract. The extract was characterized using FTIR and gas chromatography mass spectrometry (GC-MS), which identified various organic compounds, including carboxylic acids, terpene metabolites, and carbohydrates. Therefore, the extraction method herein used was efficient in extracting organic compounds, especially polyphenolics, which are believed to be responsible for the reduction of Fe^{2+} to Fe^0 .

The X-ray diffractogram of the FeNPs is shown in Figure 2, revealing the presence of different iron-containing structures in the suspension, such as hematite, goethite, and zero-valent iron. The peak at $2\theta = 45.1^\circ$ corresponds to zero-valent iron ($\alpha\text{-Fe}$), while the peaks at $2\theta = 18.5^\circ$ and $2\theta = 22.2^\circ$ can be attributed to goethite ($\alpha\text{-FeO}$). Additionally, the peaks at $2\theta = 23.6^\circ$ and $2\theta = 27.3^\circ$ correspond to hematite ($\alpha\text{-Fe}_2\text{O}_3$), and the peak at $2\theta = 33.9^\circ$ can be attributed to magnetite (Fe_3O_4). These findings are consistent with those of Puiatti *et al.*¹⁷

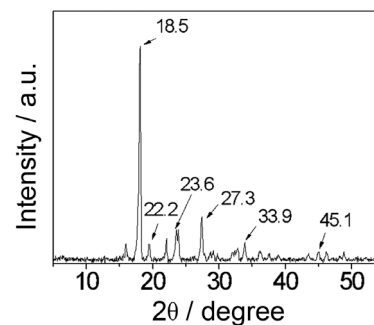


Figure 2. X-ray diffractogram of FeNPs (iron nanoparticles) synthesized through a green process utilizing *Eucalyptus grandis* leaf extract.

The morphology of the FeNPs was examined using SEM, which revealed their spherical shape (Figure S6, SI section). The TEM images of nanomaterial showed that the organic compounds present in the sample allowed the effective dispersion of the FeNPs (darker color) in a carbonaceous matrix (gray color), preventing their aggregation (Figure 3a). The presence of the carbonaceous matrix also confirms the incorporation of the extract

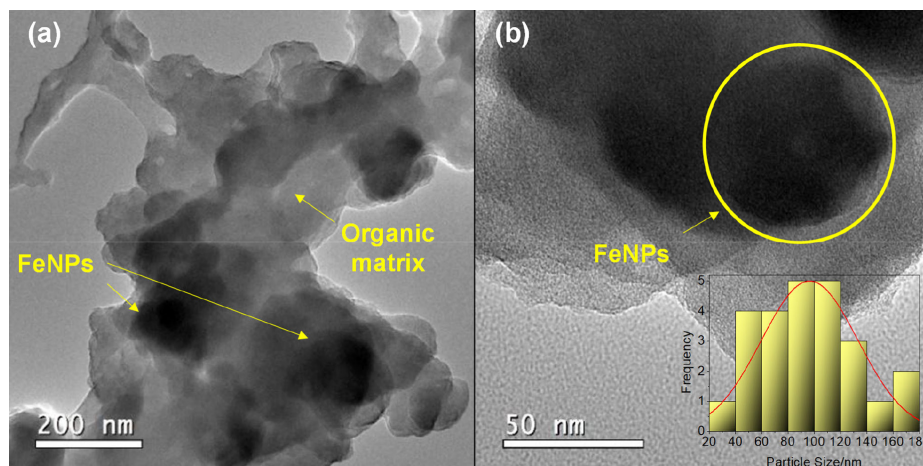


Figure 3. Transmission electron microscopy (TEM) of FeNPs (iron nanoparticles) synthesized through a green process utilizing *Eucalyptus grandis* leaf extract (a) FeNPs stabilized by the organic matrix; (b) FeNPs size.

compounds into the FeNPs' structure. The TEM image also confirmed the spherical shape of the FeNPs, which presented an average size of (96.4 ± 36.8) nm (Figure 3b). The size distribution is also shown in Figure 3b. Similar results have been reported in other works.³¹⁻³³ The catalytic activity of a material is influenced by its size. Smaller material sizes lead to a larger contact surface area between the catalyst and the substrate, resulting in an increase of activity.^{34,35}

The hydrodynamic size of the material measured by DLS was approximately 200 nm (Figure S7, SI section). It is important to note that the hydrodynamic size differs from the material's actual size. This distinction arises because DLS reveals the hydrodynamic size distribution of small particles, which encompasses both the core size and the materials used to encapsulate it. Comparable findings were achieved by Al-Karagoly *et al.*,³⁶ who synthesized iron oxide nanoparticles employing *Nigella sativa* seed extract.

The EDS result for the FeNPs is presented in Figure 4, which shows that the material is primarily composed of carbon (59.6%) due to the stabilizing phytochemicals,

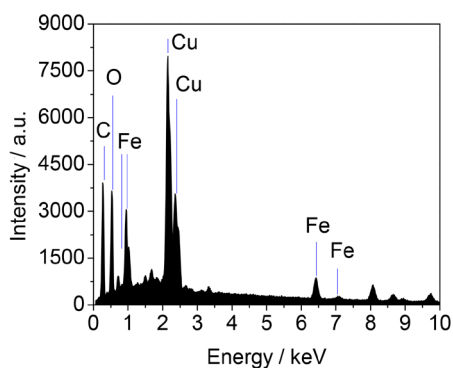


Figure 4. Energy dispersion X-ray spectrum of FeNPs (iron nanoparticles) synthesized through a green process utilizing *Eucalyptus grandis* leaf extract.

followed by oxygen (34.2%) and iron (6.2%). The presence of copper can be observed, which can be attributed to the sample holder.

The thermogravimetric analysis results are shown in Figure S8 (SI section). Thermal events can be observed in three distinct ranges: region I (30-220 °C), which is attributed to water presence; region II (220-473 °C), and region III (473-900 °C), both attributed to organic compound decomposition. These results closely resemble those obtained by Carvalho and Carvalho,³⁷ who synthesized iron nanoparticles using *Camellia sinensis* tea extract. It can be observed that the residual mass was approximately 30%, attributed to FeNPs, which agrees with the results obtained by EDS.

Application of FeNPs as peroxidase-like catalyst

Optimization of the reaction conditions

The effect of pH on the OPD oxidation was investigated by conducting experiments at pH 3.00, 5.00, and 7.00 (Figures 5 and S9, SI section). Due to the DAP formation, it is possible to observe an increase in absorbance at $\lambda = 451$ nm. The reaction occurred more efficiently at pH 3.00, as seen in Figure 5. Horseradish peroxidase is commonly used in analytical assays, but it is sensitive to pH conditions below 3.5. Therefore, it is promising that this work could expand the pH range in which OPD can be oxidized compared to the enzyme.³⁸ The system reached equilibrium at ca. 30 min, as shown by the plateau in the graph (insert of Figure 5). Different batches of iron nanoparticles (FeNPs) were synthesized, obtaining the same behavior.

The dosage of FeNPs was also evaluated (Figure S10a, SI section). Better results were observed with the increase in the catalyst dose. This occurs due to the increase of

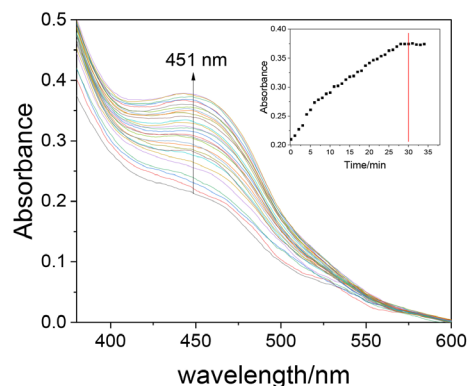


Figure 5. UV-Vis spectra of the *o*-phenylenediamine oxidation mediated by FeNPs (iron nanoparticles). Experimental conditions: 200 μL of OPD solution (10.0 mmol L^{-1}), 100 μL of H_2O_2 30% (v/v), 2.85 mL of citrate buffer pH 3, 250 μL of FeNPs suspension ($4.165 \text{ mmol L}^{-1}$). Insert: the absorbance as a function of time at $\lambda = 451 \text{ nm}$.

active sites available to react with OPD. The catalyst dose chosen was $0.306 \text{ mmol L}^{-1}$ due to higher absorbance values at 451 nm. There were no significant changes in absorbance above this value, which may be attributed to the aggregation of the nanoparticles, resulting in reduced contact with the substrate.

The OPD concentration was also evaluated (Figure S10b). The Michaelis-Menten model was fit to the experimental data. The model quality was assessed by the coefficient of correlation (R^2), which is higher than 0.9. The maximum velocity (V_{max}) and the Michaelis-Menten constant (K_m) were determined as being $2.0 \times 10^{-6} \text{ mol L}^{-1} \text{ s}^{-1}$ and $307 \text{ }\mu\text{mol L}^{-1}$, respectively. The higher the V_{max} value, the higher the catalyst activity. On the other hand, the lower the K_m , the greater the binding affinity of the substrate for the catalyst.^{39,40} The constants found in this work can be compared to other nanomaterials and horseradish peroxidase, as shown in Table 2.

As seen in Table 2, the apparent K_m value obtained by FeNPs was comparable to other works. It is important to

emphasize that the result obtained is practically half of the K_m value of horseradish peroxidase, the most commercially available peroxidase. This result indicates a high affinity of the catalyst with the substrate OPD. In addition, the FeNPs also showed a higher apparent V_{max} value than the other works, only lower than horseradish peroxidase, indicating excellent catalytic performance.

Control assays were performed, with the reaction being conducted with and without the FeNPs suspension. The results are shown in the Figure S11 (SI section). It is possible to observe that without FeNPs, after 30 min, the absorption band at 451 nm was not formed. In addition, the yellow color, characteristic of DAP, was not formed either. It can be concluded that the DAP was not formed and that the catalyst is important in the process.

Development of H_2O_2 quantification method

Based on the optimized parameters, the system was used to detect and quantify H_2O_2 in an aqueous system. For this, an analytical curve was constructed varying the H_2O_2 concentration, and the results are shown in Figure 6.

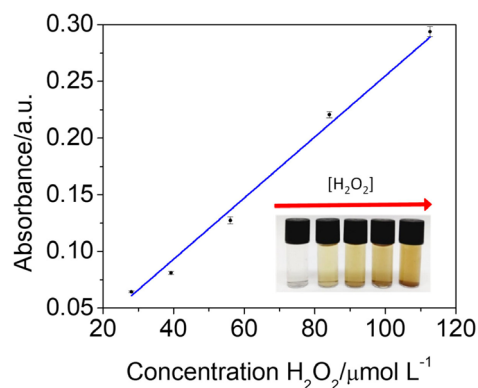


Figure 6. Analytical curve for determination of H_2O_2 obtained from *o*-phenylenediamine oxidation mediated by FeNPs (iron nanoparticles) synthesized through a green process utilizing *Eucalyptus grandis* leaf extract.

Table 2. Apparent Michaelis-Menten constant (K_m) and maximum velocity (V_{max}) obtained for different peroxidase-like nanomaterials using *o*-phenylenediamine as the substrate and horseradish peroxidase

	Catalyst	$K_m^a / (\mu\text{mol L}^{-1})$	$V_{\text{max}} / (\text{mol L}^{-1} \text{ s}^{-1})$	Reference
Peroxidase	horseradish peroxidase (pH 6.0)	600 ± 200	$6.5 \pm 1.5 \times 10^{-6}$	41
	FeNPs (pH 3.0)	307	2.00×10^{-6}	this work
	CS-nFs	143	1.01×10^{-6}	42
	Fe_3O_4 NPs/MIL-53(Al) (pH 6.5)	181	8.10×10^{-7}	6
Peroxidase-like nanomaterials	Cu-CDs + Fe^{2+} (pH 7.0)	644	4.96×10^{-8}	43
	gNPs@ Fe_3O_4 (pH 7.4)	2910	–	44
	MnFe_2O_4 (pH 7.0)	27500	1.04×10^{-7}	10
	mesoporous MnCo_2O_4 (pH 7.0)	272000	1.00×10^{-7}	45

^aAll reactions were carried out at room temperature. FeNPs: iron nanoparticles; CS-nFs: CoSe_2 nanoflakes; Fe_3O_4 NPs/MIL-53(Al): magnetically Fe_3O_4 nanoparticles based aluminium metal center containing metal organic framework; Cu-CDs + Fe^{2+} : carbon dots with Cu^+ + Fe^{2+} ; gNPs@ Fe_3O_4 : core-shell magnetite-silver nanostructures; MnFe_2O_4 : MnFe_2O_4 nanoparticles; mesoporous MnCo_2O_4 : mesoporous manganese cobaltite.

The linear regression model fits the data well, with an R^2 value of 0.9914. Besides, from the residuals plot (Figure S12, SI section), it is possible to observe the homoscedasticity of the data. The LOD, LOQ and AnR are also shown in Table 3.

The determined parameters were compared with others works reported in the literature,⁴⁶⁻⁵⁹ as shown in Table 4. The LOD for H_2O_2 was similar to other works. Furthermore, to our knowledge, this is the first time that FeNPs produced by a plant extract are used in a peroxidase-like reaction. Other nanomaterials synthesized through the green method for peroxide detection are shown in Table S1 (SI section). As can be observed, the results obtained in this study are comparable to those documented in the existing literature. This is an interesting development, as iron is inexpensive, readily available, and generally regarded as non-toxic. These findings pave the way for developing new strategies for synthesizing more sensitive green FeNPs. The present work presents LOD comparable to the others works, which indicates that FeNPs obtained by extract

of *Eucalyptus grandis* leaf can be used as a catalyst in reactions of the peroxidase-like.

Mechanism of the reaction

Peroxidases are heme proteins that commonly feature protoporphyrin IX as a prosthetic group. In the case of horseradish peroxidase, for example, the catalytic mechanism involves H_2O_2 interaction with the Fe^{3+} nucleus, formation of highly oxidized iron states (Fe^{4+}), and production of Fe^{2+} bound to oxygen.⁶⁰ To understand the mechanism of OPD oxidation catalyzed by the synthesized FeNPs, experiments were performed in the presence and absence of radical inhibitors. Methanol, ethanol, *t*-butyl alcohol and isopropyl alcohol were used to inhibit the $\cdot OH$ radicals, while sodium azide was used to evaluate the inhibition of the singlet oxygen (1O_2).⁶¹⁻⁶³ The results are shown in Figures S13 and S14 (SI section). It is possible to observe a lower absorbance value at 451 nm in the presence of methanol if compared with the other inhibitors. The

Table 3. Parameters obtained for H_2O_2 quantification by *o*-phenylenediamine oxidation mediated by FeNPs (iron nanoparticles)

Analytical curve	LOD / ($\mu mol L^{-1}$)	LOQ / ($\mu mol L^{-1}$)	AnR / ($\mu mol L^{-1}$)
$A = (-0.02754 \pm 0.529 + (0.0029 \pm 0.00103) [H_2O_2])$	5.48	18.3	0.0266

LOD: limit of detection; LOQ: limit of quantification; AnR: analytical resolution.

Table 4. Comparison of different nanomaterials that mimic peroxidase for H_2O_2 detection

Material	Linear range / ($\mu mol L^{-1}$)	LOD / ($\mu mol L^{-1}$)	Reference
Fe-NPs	18.3-112.6	5.48	this work
$Co_4N@NC$	1-100	0.032	46
$SiO_2@TiO_2/PDI-OH$	0.2-40	0.0760	47
$h-Fe_3O_4@ppy$	0.2-100	0.18	48
Cu. Cl-CDs	1-600	0.35	40
$Fe/FeS_2@C$	2-1000	0.42	49
SDBS-Cu-Cu Fe_2O_4 NPs	1.5-60	0.49	50
Ir NPs	1-100	0.53	51
$FeS@CNs$	5-250	0.78	52
FeS_2 NPs	2-200	0.91	53
$MoS_2@MgFe_2O$	2.5-300	1.00	54
N-GQDs	20-1170	5.3	55
FePt-Au HNPs	20-700	12.3	56
M-CQDs	20-200	15	57
Fe_7S_8	0.5-150	24.7	58
Pt/NiCo-LDH NCs	10.000-90.000	760	59

LOD: limit of detection; FeNPs: iron nanoparticles; $Co_4N@NC$: hollow porous N-doped carbon-based Co_4N ; $SiO_2@TiO_2/PDI-OH$: $SiO_2@TiO_2$ yolk-shell nanospheres; $h-Fe_3O_4@ppy$: magnetic ternary nanocomposite hemin- $Fe_3O_4@$ polypyrrole; Cu. Cl-CDs: Cu, Cl-doped carbon dots; $Fe/FeS_2@C$: core-shell $Fe/FeS_2@C$ nanoparticles; SDBS-Cu-Cu Fe_2O_4 NPs: surface of Cu-Cu Fe_2O_4 modified by sodium dodecyl benzene sulfonate (SDBS); Ir NPs: iridium nanoparticles; $FeS@CNs$: FeS nanoparticles embedded in 2D carbon nanosheets; FeS_2 NPs: FeS_2 nanoparticles; $MoS_2@MgFe_2O$: flower-like MoS_2 -decorated $MgFe_2O_4$ nanocomposite; N-GQDs: nitrogen-doped graphene quantum dots; FePt-Au HNPs: FePt-Au ternary metallic nanoparticles; M-CQDs: Mustard seeds derived fluorescent carbon quantum dots; Fe_7S_8 : Fe_7S_8 nanowires templated from $[Fe_{16}S_{20}]/$ diethylenetriamine hybrid nanowires; Pt/NiCo-LDH NCs: Pt deposited on NiCo layered double hydroxide.

highest percentage inhibition was for methanol (71.1%), followed by ethanol (63.7%), isopropyl alcohol (39.2%), sodium azide (28.4%) and *t*-butyl alcohol (10.9%). Therefore, four kinds of reactive oxide species play a key role in the oxidation of OPD to form DAP.

XRD is an important technique to elucidate the catalyst composition. As previously mentioned, the FeNPs are composed of hematite, goethite, and zero-valent iron. Based on these results, Figure 7 presents a possible mechanism for the reaction, with the first step based on Guan *et al.*⁶⁴ According to this mechanism, H₂O₂ molecules adsorb onto the surface of the FeNPs, followed by the activation and homolytic cleavage of the peroxide bond, generating ·OH radicals. The subsequent steps outline a general path for radical reactions. These steps may involve hydrogen abstraction by ·OH radicals, oxidative coupling of the molecules, and elimination reactions.

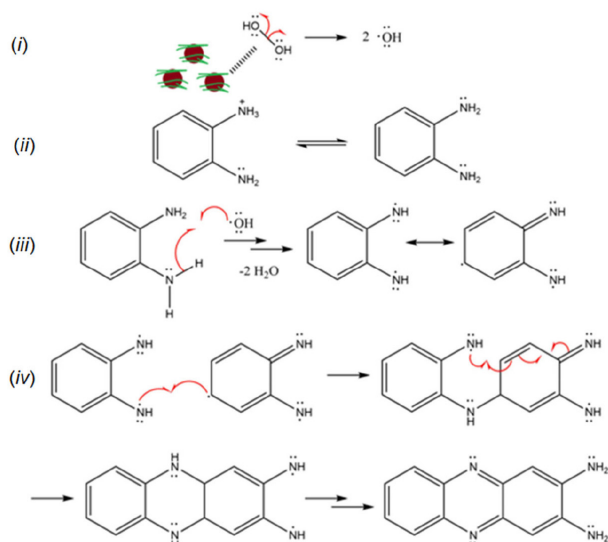


Figure 7. Proposed mechanism for the catalytic oxidation of OPD in the presence of H₂O₂ mediated by FeNPs synthesized from *Eucalyptus grandis* leaf extract. (i) Adsorption of H₂O₂ onto the catalyst; (ii) acid-base equilibrium of OPD in aqueous solution; (iii) hydrogen abstraction; (iv) oxidative coupling, followed by prototropism and elimination to form DAP.

Conclusions

Eucalyptus grandis extract was used as a stabilizing and reducing agent for the synthesis of FeNPs in a simple, bio-inspired, and environmentally friendly way. FTIR, SEM, TEM, and EDS analysis confirmed the formation of the nanoparticles and the incorporation of the extract components into their structure. The FeNPs were then applied as catalysts in the *o*-phenylenediamine oxidation by H₂O₂. It was possible to develop an easy and effective spectrophotometric method for determining H₂O₂ that presented limits of detection and quantification comparable

to the literature. The FeNPs synthesized presented peroxidase-like activity, being cheaper and easier to produce than the natural enzymes.

Supplementary Information

Supplementary information is available free of charge at <http://jbcs.sbq.org.br> as PDF file.

Acknowledgments

The authors thank the Coordenação de Aperfeiçoamento de Pessoal de Nível Superior - Brazil (CAPES), Conselho Nacional de Desenvolvimento Científico e Tecnológico (CNPq); process: 312400/2021-7 and 405828/2022-5, Fundação de Amparo à Pesquisa do Estado de Minas Gerais; process: FAPEMIG RED-00144-22 and FAPEMIG APQ-01275-18, Department of Chemistry of Universidade Federal de Viçosa, Department of Physics of Universidade Federal de Viçosa, and the Center of Microscopy at the Universidade Federal de Minas Gerais for providing the equipment and technical support for experiments involving electron microscopy.

Author Contributions

Luísa F. M. Mazzini was responsible for the conceptualization, data curation, formal analysis, investigation, validation, visualization, writing of the original draft; Guilherme Mateus Bousada for the formal analysis, investigation, writing-review and editing; Gustavo A. Puiatti writing-review and editing; Renata P. L. Moreira formal analysis, funding acquisition, investigation, writing-review and editing.

References

- Peng, L. J.; Zhou, H. Y.; Zhang, C. Y.; Yang, F. Q.; *Colloids Surf., A* **2022**, *647*, 129031. [Crossref]
- Yu, Y.; Pan, M.; Peng, J.; Hu, D.; Hao, Y.; Qian, Z.; *Chin. Chem. Lett.* **2022**, *33*, 4133. [Crossref]
- Zhu, L.; Luo, M.; Zhang, Y.; Fang, F.; Li, M.; An, F.; Zhao, D.; Zhang, J.; *Coord. Chem. Rev.* **2023**, *475*, 214875. [Crossref]
- Jangi, S. R. H.; Davoudli, H. K.; Delshad, Y.; Jangi, M. R. H.; Jangi, A. R. H.; *Surf. Interfaces* **2020**, *21*, 100771. [Crossref]
- Itel, F.; Schattling, P. S.; Zhang, Y.; Städler, B.; *Adv. Drug Delivery Rev.* **2017**, *118*, 94. [Crossref]
- Chakraborty, A.; Acharya, H.; *Colloids Surf., A* **2021**, *624*, 126830. [Crossref]
- Xu, C.; Zhou, J.; Ye, Y.; Tang, B.; *Spectrochim. Acta, Part A* **2021**, *262*, 120083. [Crossref]

8. Uzunboy, S.; Avan, A. N.; Demirci-Çekiç, S.; Apak, R.; *Microchem. J.* **2022**, *178*, 107335. [Crossref]
9. Liang, M.; Yan, X.; *Acc. Chem. Res.* **2019**, *52*, 2190. [Crossref]
10. Vetr, F.; Moradi-Shoeili, Z.; Özkaz, S.; *Appl. Organomet. Chem.* **2018**, *32*, 4465. [Crossref]
11. Monga, Y.; Kumar, P.; Sharma, R. K.; Filip, J.; Varma, R. S.; Zbořil, R.; Gawande, M. B.; *ChemSusChem* **2020**, *13*, 3288. [Crossref]
12. Selvaraj, R.; Pai, S.; Vinayagam, R.; Varadavenkatesan, T.; Kumar, P. S.; Duc, P. A.; Rangasamy, G.; *Chemosphere* **2022**, *308*, 136331. [Crossref]
13. Xu, W.; Yang, T.; Liu, S.; Du, L.; Chen, Q.; Li, X.; Dong, J.; Zhang, Z.; Lu, S.; Gong, Y.; Zhou, L.; Liu, Y.; Tan, X.; *Environ. Int.* **2022**, *158*, 10980. [Crossref]
14. Huang, J.; Lin, L.; Sun, D.; Chen, H.; Yang, D.; Li, Q.; *Chem. Soc. Rev.* **2015**, *44*, 6330. [Crossref]
15. Mondal, P.; Anweshan, A.; Purkait, M. K.; *Chemosphere* **2020**, *259*, 127509. [Crossref]
16. Muzafar, W.; Kanwal, T.; Rehman, K.; Perveen, S.; Jabri, T.; Qamar, F.; Faizi, S.; Shah, M. R.; *J. Mol. Struct.* **2022**, *1269*, 133824. [Crossref]
17. Puiatti, G. A.; de Carvalho, J. P.; de Matos, A. T.; Lopes, R. P.; *J. Environ. Manage.* **2022**, *311*, 114828. [Crossref]
18. Rasband, W. S.; *ImageJ*, version 1.51k; U. S. National Institutes of Health, Bethesda, Maryland, USA, 2017.
19. Zakariya, N. A.; Majeed, S.; Jusof, W. H. W.; *Sens. Int.* **2022**, *3*, 100164. [Crossref]
20. Wang, N.; Hsu, C.; Zhu, L.; Tseng, S.; Hsu, J. P.; *J. Colloid Interface Sci.* **2013**, *407*, 22. [Crossref]
21. Lopes, R. P.; Guimarães, T.; Moro, M. M.; Guisasola, E.; Moya, S.; Astruc, D.; *Waste Biomass Valorization* **2022**, *13*, 3629. [Crossref]
22. Goddeti, S. M. R.; Bhaumik, M.; Maity, A.; Ray, S. S.; *Int. J. Biol. Macromol.* **2020**, *149*, 21. [Crossref]
23. Shi, B.; Gao, S.; Yu, H.; Zhang, L.; Song, C.; Huang, K.; *React. Funct. Polym.* **2020**, *153*, 104614. [Crossref]
24. Azoulay, I.; Rémazeilles, C.; Refait, P.; *Corros. Sci.* **2012**, *58*, 229. [Crossref]
25. Cook, W. G.; Olive, R. P.; *Corros. Sci.* **2012**, *55*, 326. [Crossref]
26. Wang, T.; Jin, X.; Chen, Z.; Megharaj, M.; Naidu, R.; *Sci. Total Environ.* **2014**, *466-467*, 210. [Crossref]
27. Ji, Y.; *Colloids Surf., A* **2014**, *444*, 1. [Crossref]
28. Moreno-Castilla, C.; Naranjo, A.; López-Ramón, M. V.; Siles, E.; López-Peñalver, J. J.; de Almodóvar, J. M. R.; *J. Catal.* **2022**, *414*, 179. [Crossref]
29. Pabón, S. E.; Benítez, R. B.; Villa, R. A. S.; Corredor, J. A. G.; *Heliyon* **2022**, 11429. [Crossref]
30. Oliveira, L. M. F.; da Silva, U. P.; Braga, J. P. V.; Teixeira, Á. V. N. C.; Ribon, A. O. B.; Varejão, E. V. V.; Coelho, E. A. F.; de Freitas, C. S.; Teixeira, R. R.; Moreira, R. P. L.; *J. Braz. Chem. Soc.* **2023**, *34*, 527. [Crossref]
31. Qiang, C.; Zhang, L.; He, H.; Liu, Y.; Zhao, Y.; Sheng, T.; Liu, S.; Wu, X.; Fang, Z.; *J. Colloid Interface Sci.* **2021**, *604*, 650. [Crossref]
32. Truskewycz, A.; Shukla, R.; Ball, A. S.; *J. Environ. Chem. Eng.* **2016**, *4*, 4409. [Crossref]
33. Wu, Y.; Chen, J. Y.; He, W. M.; *Sens. Actuators, B* **2022**, *365*, 131939. [Crossref]
34. You, S. M.; Park, J. S.; Luo, K.; Jeong, K. B.; Adra, H. J.; Kim, Y. R.; *Carbohydr. Polym.* **2021**, *267*, 11816. [Crossref]
35. Uzunoglu, D.; Özer, A.; *J. Environ. Chem. Eng.* **2023**, *11*, 109159. [Crossref]
36. Al-Karagoly, H.; Rhyaf, A.; Naji, H.; Albukhaty, S.; Almalki, F. A.; Alyamani, A. A.; Albaqami, J.; Aloufi, S.; *Green Process. Synth.* **2022**, *11*, 254. [Crossref]
37. Carvalho, S. S. F.; Carvalho, N. M. F.; *J. Environ. Manage.* **2017**, *187*, 82. [Crossref]
38. Drozd, M.; Pietrzak, M.; Parzuchowski, P. G.; Malinowska, E.; *Anal. Bioanal. Chem.* **2016**, *408*, 8505. [Crossref]
39. Zhang, L.; Wang, J.; Zhao, C.; Zhou, F.; Yao, C.; Song, C.; *Sens. Actuators, B* **2022**, *361*, 131750. [Crossref]
40. Zhao, N.; Song, J.; Zhao, L.; *Colloids Surf., A* **2022**, *648*, 129390. [Crossref]
41. Hamilton, T. M.; Dobie-Galuska, A. A.; Wietstock, S. M.; *J. Chem. Educ.* **1999**, *76*, 642. [Crossref]
42. Warkhade, S. K.; Singh, R. P.; Das, R. S.; Gaikwad, G. S.; Zodape, S. P.; Pratap, U. R.; Maldhure, A.; Wankhade, A. V.; *Inorg. Chem. Commun.* **2021**, *126*, 108461. [Crossref]
43. Yang, D.; Li, Q.; Tammina, S. K.; Gao, Z.; Yang, Y.; *Sens. Actuators, B* **2020**, *319*, 128273. [Crossref]
44. Mazhani, M.; Alula, M. T.; Murape, D.; *Anal. Chim. Acta* **2020**, *1107*, 193. [Crossref]
45. Vetr, F.; Moradi-Shoeili, Z.; Özkaz, S.; *Inorg. Chem. Commun.* **2018**, *98*, 184. [Crossref]
46. Tao, N.; Xu, Y.; Wang, L.; Yang, W.; Liu, Y.-N.; *Microchem. J.* **2021**, *166*, 106206. [Crossref]
47. Liu, Q.; Cao, S.; Sun, Q.; Xing, C.; Gao, W.; Lu, X.; Li, X.; Yang, G.; Yu, S.; Chen, Y.; *J. Hazard. Mater.* **2022**, *436*, 129321. [Crossref]
48. Yang, W.; Weng, C.; Li, X.; He, H.; Fei, J.; Xu, W.; Yan, X.; Zhu, W.; Zhang, H.; Zhou, X.; *Sens. Actuators, B* **2021**, *338*, 129844. [Crossref]
49. Zhao, C.; Shi, G. M.; Shi, F. N.; Wang, X. L.; Li, S. T.; *Colloids Surf., A* **2022**, *642*, 128612. [Crossref]
50. Xia, F.; Shi, Q.; Nan, Z.; *Surf. Interfaces* **2021**, *24*, 101109. [Crossref]
51. Cui, M.; Zhou, J.; Zhao, Y.; Song, Q.; *Sens. Actuators, B* **2017**, *243*, 203. [Crossref]
52. Song, C.; Liu, H.; Zhang, L.; Wang, J.; Zhao, C.; Xu, Q.; Yao, C.; *Sens. Actuators, B* **2022**, *353*, 131131. [Crossref]
53. Song, C.; Ding, W.; Zhao, W.; Liu, H.; Wang, J.; Yao, Y.; Yao, C.; *Biosens. Bioelectron.* **2020**, *151*, 111983. [Crossref]

54. Zhang, Y.; Zhou, Z.; Wen, F.; Tan, J.; Peng, T.; Luo, B.; Wang, H.; Yin, S.; *Sens. Actuators, B* **2018**, 275, 155. [Crossref]
55. Lin, L.; Song, X.; Chen, Y.; Rong, M.; Zhao, T.; Wang, Y.; Jiang, Y.; Chen, X.; *Anal. Chim. Acta* **2015**, 869, 89. [Crossref]
56. Ding, Y.; Yang, B.; Liu, H.; Liu, Z.; Zhang, X.; Zheng, X.; Liu, Q.; *Sens. Actuators, B* **2018**, 259, 775. [Crossref]
57. Chandra, S.; Singh, V. K.; Yadav, P. K.; Bano, D.; Kumar, V.; Pandey, V. K.; Talat, M.; Hasan, S. H.; *Anal. Chim. Acta* **2019**, 1054, 145. [Crossref]
58. Yao, W. T.; Zhu, H. Z.; Li, W. G.; Yao, H. Bin; Wu, Y. C.; Yu, S. H.; *ChemPlusChem* **2013**, 78, 723. [Crossref]
59. Cao, X.; Yang, H.; Wei, Q.; Yang, Y.; Liu, M.; Liu, Q.; Zhang, X.; *Inorg. Chem. Commun.* **2021**, 123, 108331. [Crossref]
60. de Oliveira, F. K.; Santos, L. O.; Buffon, J. G.; *Food Res. Int.* **2021**, 143, 110266. [Crossref]
61. Chen, X.; Oh, W. D.; Lim, T. T.; *Chem. Eng. J.* **2018**, 354, 941. [Crossref]
62. Guo, R.; Xi, B.; Guo, C.; Liu, W.; Lv, N.; Xu, J.; *Environ. Funct. Mater.* **2022**, 1, 239. [Crossref]
63. Ji, Y.; Ferronato, C.; Salvador, A.; Yang, X.; Chovelon, J. M.; *Sci. Total Environ.* **2014**, 472, 800. [Crossref]
64. Guan, J.; Peng, J.; Jin, X.; *Anal. Methods* **2015**, 7, 5454. [Crossref]

Submitted: May 13, 2023

Published online: October 26, 2023